

Earth and Space Science



RESEARCH ARTICLE

10.1029/2022EA002252

Key Points:

- Rock abundance of ~5% identified at Zhurong landing site from orbital and ground measurements
- Rock breakdown and surface denudation rate at Zhurong landing site and its neighboring region are estimated
- Low erosion rates suggest an arid climate in the Amazonian period

Supporting Information:

Supporting Information may be found in the online version of this article.

Correspondence to:

B. Wu,
bo.wu@polyu.edu.hk

Citation:

Chen, Z., Wu, B., Wang, Y., Liu, S., Li, Z., Yang, C., et al. (2022). Rock abundance and erosion rate at the Zhurong landing site in southern Utopia Planitia on Mars. *Earth and Space Science*, 9, e2022EA002252. <https://doi.org/10.1029/2022EA002252>




Received 20 JAN 2022

Accepted 29 JUN 2022

Author Contributions:

Conceptualization: Zeyu Chen, Bo Wu
Data curation: Yiran Wang, Shuo Liu, Zhaojin Li, Chenyu Yang
Methodology: Zeyu Chen, Bo Wu
Resources: Jie Dong, Wei Rao
Supervision: Bo Wu
Validation: Jie Dong, Wei Rao
Writing – original draft: Zeyu Chen
Writing – review & editing: Bo Wu, Yiran Wang

Rock Abundance and Erosion Rate at the Zhurong Landing Site in Southern Utopia Planitia on Mars

Zeyu Chen¹ , Bo Wu¹ , Yiran Wang¹, Shuo Liu¹, Zhaojin Li¹ , Chenyu Yang¹, Jie Dong², and Wei Rao²

¹Planetary Remote Sensing Laboratory, Department of Land Surveying and Geo-Informatics, The Hong Kong Polytechnic University, Hong Kong, China, ²China Academy of Space Technology, Beijing, China

Abstract Rocks on the Martian surface exhibit signatures of geological activities. Rock distribution is also an important factor for landing site selection for exploration missions. This study investigated the rock abundance and erosion rate at the landing site of the Chinese Mars rover, Zhurong, in southern Utopia Planitia. A convolutional neural network based method was developed for rock detection from the images (0.7 m/pixel) obtained by using the high-resolution imaging camera (HiRIC) onboard the Tianwen-1 orbiter. Approximately 10,000 rocks with a minimum diameter of 1.4 m (2 pixels on the image) were extracted from the HiRIC images covering the Zhurong landing site and its neighboring region. According to the results, the rock abundance at the Zhurong landing site was approximately 5%. Measurements from the ground images acquired by the Zhurong rover after landing confirmed a rock abundance of approximately 5% at the landing site, consistent with the orbital measurement before landing. Furthermore, we investigated the rock erosion rate at the Zhurong landing region. Rock abundance was negatively correlated with the crater retention age and positively correlated with crater diameter. The obtained rock breakdown rate (0.054 nm/y to 0.074 nm/y) and surface denudation rate by filled volume of craters (0.104 nm/y to 0.209 nm/y) were in agreement with the values previously reported for the Amazonian period on Mars. The low erosion rate implies a dry climate and the absence of fluvial erosion processes in the Amazonian period.

1. Introduction

On 15 May 2021, the Chinese Mars rover, Zhurong, onboard the Tianwen-1 spacecraft successfully landed in southern Utopia Planitia at 109.925°E and 25.066°N (Wu et al., 2022). Before this landing, the Tianwen-1 spacecraft successfully entered Mars orbit in February 2021, and investigated the candidate landing regions using its onboard high-resolution imaging camera (HiRIC) and other sensors. The rock abundance, crater density, surface slopes, and other constraints are evaluated to identify the most suitable landing site with minimum hazards (Wu et al., 2021, 2022).

Rocks are prominent geomorphological features on the Martian surface, which may pose threats to the lander and rover. Rock abundance, defined as the cumulative fractional area covered by rocks with respect to the rock diameter (typically representing rocks with a diameter ≥ 0.1 m) (Golombek & Rapp, 1997), is a key consideration for safe landing (Golombek et al., 2012; Pajola et al., 2017; Wu et al., 2018, 2020). For the ExoMars mission, the rock abundance of the candidate landing site was required to be less than 7% to avoid possible accidents (Vago et al., 2015). A rock abundance of less than 8% was required for the Mars Science Laboratory (MSL) mission (Golombek et al., 2012). For the InSight mission, the rock abundance was required to be less than 10% (Golombek et al., 2017). A rock abundance of less than 7% was applied for selecting the landing site for the Zhurong rover (Wu et al., 2021). In general, a safe landing has generally so far required a rock abundance of less than 10%.

The analysis of rock abundance on Mars usually relies on ground images collected by rovers or landers at the landing sites. Although a relationship for the size-frequency distribution of rocks on Mars has been proposed (Golombek & Rapp, 1997) and subsequently successfully applied in various missions (Golombek et al., 2003, 2006, 2021; Golombek, Warner, et al., 2020; Heet et al., 2009), this relationship cannot be directly used for landing site evaluation owing to constraints of the spatial resolutions of images acquired from the orbit. Large-scale analysis of rocks for landing site selection is usually performed through orbit thermal images, such as those obtained using the Viking infrared thermal mapper (IRTM) (Christensen, 1986) and Mars global surveyor thermal emission spectrometer (Nowicki & Christensen, 2007), based on the thermal inertia of rocks. Golombek et al. (2003) measured boulders larger than 5 m using the Mars Orbiter Camera (MOC) images, but the image resolution is a critical

© 2022 The Authors. Earth and Space Science published by Wiley Periodicals LLC on behalf of American Geophysical Union.

This is an open access article under the terms of the [Creative Commons Attribution-NonCommercial-NoDerivs License](https://creativecommons.org/licenses/by/4.0/), which permits use and distribution in any medium, provided the original work is properly cited, the use is non-commercial and no modifications or adaptations are made.

constraint. The availability of high-resolution orbital images, for example, high-resolution imaging experiment (HiRISE) images (0.25 m/pixel) and HiRIC images (0.7 m/pixel), can facilitate the analysis of the rock abundance at a submeter scale. To perform rock analyses through such methods, rocks must be automatically detected from the large volume of high-resolution orbital images. Golombek et al. (2008) developed an automatic rock detection algorithm based on the shadow cast from rocks, which was successfully applied for the landing site evaluation for the Phoenix and InSight missions (Golombek et al., 2008, 2017, 2020a, 2021). Charalambous (2014) proposed a particle fragmentation theory that estimates rock abundance from crater populations and surface ages. The proposed Negative Binomial (NB) model avoided the resolution constraint for rock counting and fitted well with measurements from satellite images at the InSight landing site (Golombek et al., 2021).

Furthermore, rocks provide evidence of geological processes on Mars. Rocks of Martian regolith have multiple sources, such as impacts (Grant et al., 2006) and breakdown of bedrocks (Day & Kocurek, 2016). The dynamics of rock abundance reflect various processes, such as deflation, burying, sublimation, and fluvial transportation (Grant et al., 2004; Greeley et al., 2006; Howard et al., 2016). The abundance and distributions of rocks can be indicators of the Martian geological history (Grant et al., 2004, 2006).

This study investigated the rock abundance and erosion rate at the Zhurong landing site and its neighboring region in southern Utopia Planitia. First, a rock detection method based on convolutional neural networks (CNNs) was developed to extract the location and diameter information of rocks from the HiRIC images, followed by manual verification to generate a rock abundance map covering the study area. Second, rock size-frequency distributions were estimated from the ground images acquired by the Zhurong rover after landing, and the rock abundance values from in situ measurements were compared with the orbital measurements. Third, the rock abundance values associated with craters of different ages and diameters were analyzed. The rock breakdown and surface denudation rates at the Zhurong landing site and neighboring region were derived. Finally, the results are discussed, and concluding remarks are presented.

2. Rock Detection Method

2.1. CNN-Based Rock Detection Method

Figure 1 shows the workflow of the CNN-based method developed for rock extraction from high-resolution images. The process involves three steps. The first step involves upsampling the original images by four times to obtain super-resolution images using a generative adversarial network (GAN) to increase the detection accuracy (Goodfellow et al., 2014). Subsequently, a refined CNN-based object detection network is used to select regions of interest (ROIs) of rocks from the super-resolution images. The ROI selection network contains three output heads of different scales to detect ROI candidates. All the candidates are extracted for ellipse fitting. The third step involves detecting and labeling the rock boundaries by using an ellipse fitting algorithm to calculate the rock diameter. During ellipse fitting, the ROIs are abandoned if the fitted ellipses are excessively large or the rock boundaries cannot be identified. Rocks are labeled using ellipses, and then their center coordinates, axes, and dimensions are recorded in a shapefile. The extracted results are evaluated considering the HiRIC images through manual labels and ground images acquired by Viking-2 (VL2), Pathfinder (MPF), and InSight rovers.

2.1.1. Training Data Set and Super-Resolution Image Enhancement

A training data set containing the images and corresponding rock ROIs were established to train the CNN for detecting ROI candidates from images. The data set was established using high-resolution HiRISE images extracted in southern Utopia Planitia, by using the ArcMap software. Before selecting the training data, the images were recovered using the enhanced super-resolution generative adversarial network (ESRGAN) algorithm (Wang et al., 2019) to increase the spatial resolution of the images by four times. The upsampled images were subsequently used as input images to the CNN. In contrast to traditional upsampling methods such as bilinear and cubic interpolation, which cannot intelligently recognize texture and patterns and are vulnerable to blurring, the ESRGAN algorithm increases the spatial resolution while maintaining sharp details. Image information is shown in Table 1.

The boundaries of rocks and boulders were manually labeled. Only the RGB parts of the HiRISE images were used as training data to enhance the accuracy of manual labeling. The region of the bounding boxes was determined by the length of the sunlit sides and shadows. All distinctive rock features were labeled, although several

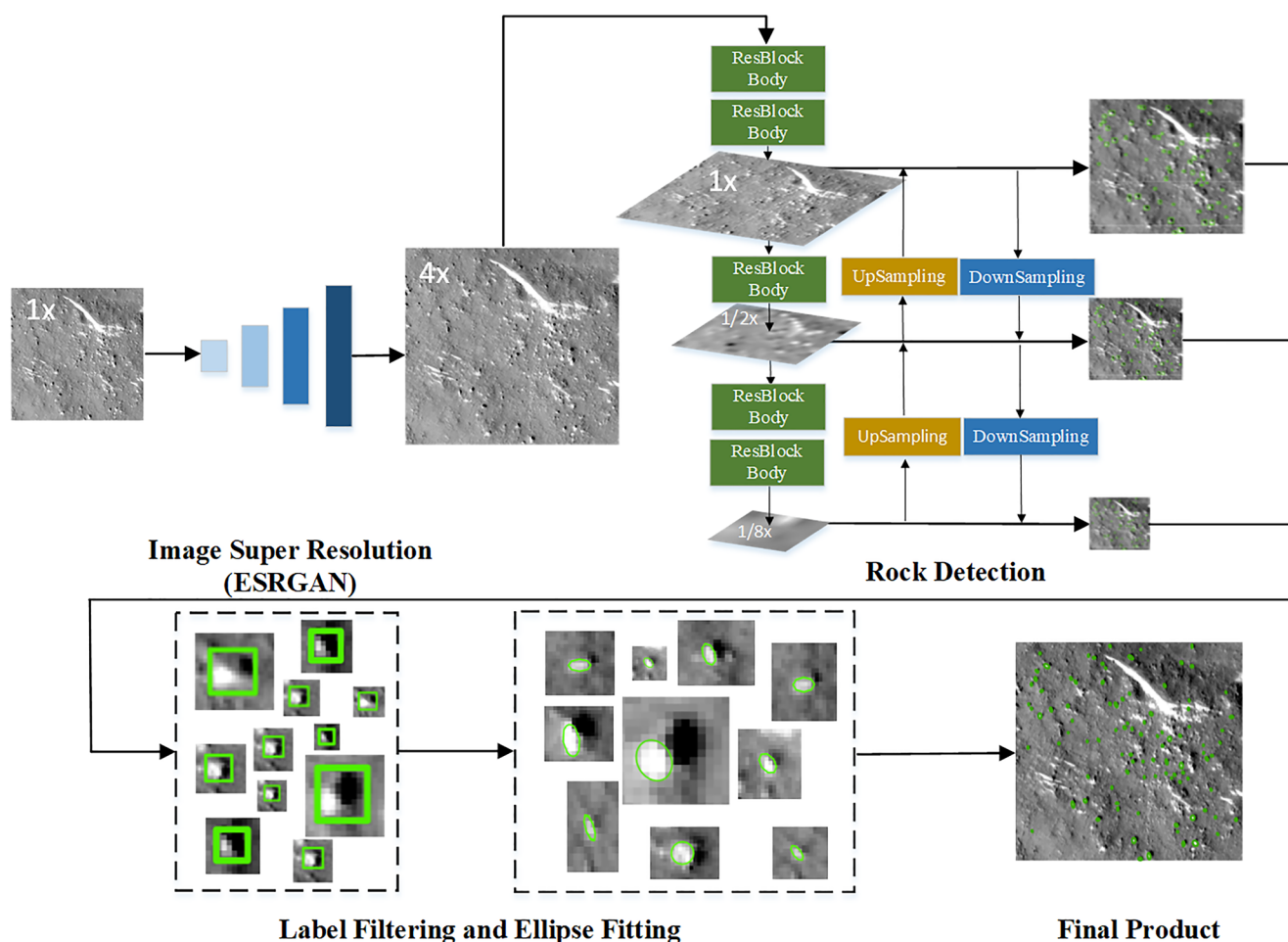


Figure 1. Workflow of the convolutional neural network-based rock detection method.

of these features were expected to be outcrops and ripples. The final training data set included approximately 6,429 rock ROIs on 4,360 image patches sized 416×416 pixels. The patch size is the required input size of the designed network and would not change during prediction.

2.1.2. Rock ROI Determination Based on CNN

Rock detection from satellite images is a challenging task. Rocks on planetary surfaces have bright sunlit and dark shadow sides; this phenomenon is not unique to rocks and can be observed on many surface objects. An algorithm that retrieves rocks based on such criteria may lead to false detections, and the manual check may be highly time-intensive. CNN object detection has demonstrated considerable potential and has been extensively applied in planetary science (e.g., Yang et al., 2020). Moreover, such approaches are rendered highly efficient through graphics processing unit (GPU) acceleration.

In such applications, the efficiency and accuracy of the network must be considered. High efficiency reduces the time consumption for algorithm implementation, and high accuracy decreases the human workload by minimizing false positive detections. In this study, the YOLO-V4 network was selected as the backbone network

Table 1
Information of the High-Resolution Imaging Experiment Image Used for Generating the Training Data Set

Image ID	Spatial resolution	Central latitude	Central longitude	Emission angle	Phase angle	Incidence angle
ESP_046929_2050	0.5 m/pixel	24.639°	110.058°	2.2°	60.0°	58°

(Bochkovskiy et al., 2020). The network architecture is shown in Figure 1. It includes a series of ResBlock bodies and a PANet to incorporate information among high levels and low levels (Bochkovskiy et al., 2020). However, this network was originally designed to detect ordinary objects such as humans, bicycles, and planes, which are usually distinct in images. Following the definition of the COCO data set (Lin et al., 2014), objects smaller than 32×32 pixels were defined as small objects, and the detection of small objects is challenging. For example, in the proposed application for Mars, if the spatial resolution of an image is 0.7 m, a rock with a diameter of 1.4 m occupies only 2×2 pixels in the original image. Therefore, the proposed backbone network must be optimized. The initial network was designed to output the detected objects on three output heads with a feature size of 52×52 , 26×26 , and 13×13 pixels for an input image with a size of 416×416 pixels. In other words, the features are downsampled by 8, 16, and 32 times. The original downsampling rates were not suitable for our task. As shown in Figure 1, we adjusted the downsampling rates to sizes of 104×104 , 52×52 , and 13×13 pixels for the three output heads. In this case, because the super-resolution algorithm was applied to upsample the images by four times, a 1.4 m rock observed in the upsampled image with a spatial resolution of 0.175 m corresponds to 2×2 pixels on the first output head and one pixel on the second output head. The rock is not visible on the last output head. However, this head is not responsible for rock extraction and only provides high-level information for the other two layers. A high-resolution feature has sharp details with textural information but no high-level recognition. A low-resolution feature contains object-level features; however, small objects may be overlooked because of the low resolution. Integration of low-level and high-level features can help maximize the ability of the network to detect ROI candidates. Except for these modifications to YOLO-V4, the other network architectures corresponded to default settings.

The proposed network was implemented and trained on TensorFlow 1.14.0 on the Python platform (Abadi et al., 2016). The data set was randomly split into training and validation sets in a 0.9:0.1 ratio. The original parameter settings in YOLO-V4 (Bochkovskiy et al., 2020) were applied in this study for rock detection.

2.1.3. ROI Filtering and Ellipse Fitting of Rock Boundaries

Classification and ellipse fitting algorithms were introduced after ROI selection to accurately extract rock boundaries and filter false positive rock candidates. Pixels in ROI candidates were classified as rock pixels, background pixels, and shadows. The k-means++ clustering algorithm (Arthur & Vassilvitskii, 2007) was used to label the rocks in pixels to separate the bright and dark features and background from the ROI regions. In most cases, the three classes can be expected to be effectively classified. However, in certain ROIs, only shadows and background pixels may be detectable. In such cases, the ROI candidate is abandoned because the rock boundary cannot be identified. Moreover, ROIs are abandoned when shadows cannot be observed in the images, which implies that the detected rocks are ripples or are low in height.

The final step involved fitting ellipses for rocks to extract the rock diameters, which is the mean length of the major and minor axes of the corresponding ellipses. Notably, features of the edges of ripples and craters are similar to those of rocks. In this case, some false detections may escape from the previous filtering processes. During ellipse fitting, these false detections are often too large to be fully labeled by ROI bounding boxes, and the diameters of the fitted rock pixels are also abnormally large. Thus, the last filtering criterion was to abandon these entities.

2.2. Evaluation of the Rock Detection Approach

The evaluation involved two parts. First, the performance of the proposed algorithm was evaluated over HiRIC images and compared with the ground truth labeled by human experts. The precision and recall values were calculated as evaluation indices. In the second part, the rock detection results based on the VL2, MPF, and InSight ground images were compared with those obtained using HiRISE images through the proposed method.

The performance of the rock detection algorithm of two locations within the landing site candidate region was evaluated. Detections were defined to be true positive if the overlap between the calculated rock boundary and ground truth was larger than 50%. The precision and recall were defined as follows:

$$Precision = \frac{TP}{TP + FP}, \quad (1)$$

$$Recall = \frac{TP}{TP + FN}, \quad (2)$$

where TP represents true positive labels, FP represents false positive labels, and FN represents false negatives.

Figure 2 shows the results obtained using the proposed approach. Most of the visible and suspicious rocks are successfully detected, and the overall performance is stable for the two locations within the landing site candidate region. In terms of false detections, the percentage of false positives is higher than that of false negatives. This higher value is attributable to the fact that we adjust the threshold to detect as many suspicious rocks as possible to avoid any potential risks at landing. The strategy also enhances the efficiency of human judgment after detection. Table 2 summarizes the evaluation results. The average classification precision and recall rates are approximately 80%, which is satisfactory. Most of the false detections pertain to shadow areas and small craters. These errors can be detected and eliminated during subsequent manual verification.

Based on case studies on Viking Lander 1 (VL1) and 2 (VL2) landing sites and Earth analogs, Golombek and Rapp (1997) noted that the cumulative fractional area of rocks versus their diameter follows an exponential relationship:

$$F_k(D) = ke^{-qD}, \quad (3)$$

where D is the rock diameter, $F_k(D)$ is the cumulative fractional area (CFA) of rocks with diameters $\geq D$, k is the rock abundance within the area, and q is the exponential coefficient. $q(k)$ is negatively correlated with the rock abundance:

$$q(k) = 1.79 + 0.152/k. \quad (4)$$

The effectiveness of the coefficients has been validated over multiple Mars exploration missions (Golombek et al., 2008, 2021; Wu et al., 2021). Results demonstrate that the parameters are satisfactory. Therefore, in this study, the equations and parameters were set to have default values.

In the second part of the evaluation, VL2, MPF, and InSight ground data were used as the ground truth for comparison, and the default values in Equation 4 were used for rock abundance determination. HiRISE images (details listed in Table 3) covering the VL2, MPF and InSight landing sites were selected for rock detection using the proposed method. Golombek et al. (2008) determined that most detections with a diameter larger than 2.25 m are false positives and maybe outcrops, ejecta, small mountains, and ripples. A similar phenomenon was observed in our analysis. Therefore, we excluded rocks with diameters larger than 2.7 m in size–frequency analysis based on experimental observations.

Figure 3 shows the rock abundance at the VL2, MPF and InSight landing sites as measured from ground data and HiRISE images. Rocks with diameters ranging from 1.4 to 2.7 m in the HiRISE images within a 450 m diameter range centered at the landing site were counted using the proposed approach. The rock abundance at the VL2 and MPF landing sites measured from the ground data is approximately 14%–19%. Our measurements based on the HiRISE images yield similar values of 13%–17% for VL2 and 10%–15% for MPF. The rock abundance at the InSight landing site is 1%–5%, lower than our results between 5% and 8% measured from the HiRISE image. The inconsistencies might be explained by the fact that large rocks are not as many as small rocks and they could be confused with other objects on the surface, which have more influence on the rock abundance, especially for areas with low rock abundances (e.g., the InSight landing site). The complicated terrain situation with abundant shadows and ripples amplifies the challenges encountered by the proposed algorithm. Compared with the shadow-detection method (Golombek et al., 2012), the proposed algorithm has a similar performance to obtain an approximate estimation of rock abundance from ground images.

3. Rock Abundance at the Zhurong Landing Site

3.1. Rock Abundance Derived From HiRIC Orbital Images

The CNN-based method was used for rock detection on the HiRIC images covering the Zhurong landing site and its neighboring region, with a combined area of 274 km². The images were acquired to evaluate the landing site before landing (Wu et al., 2021). The image number of used tiles is shown in Table S1. The HiRIC

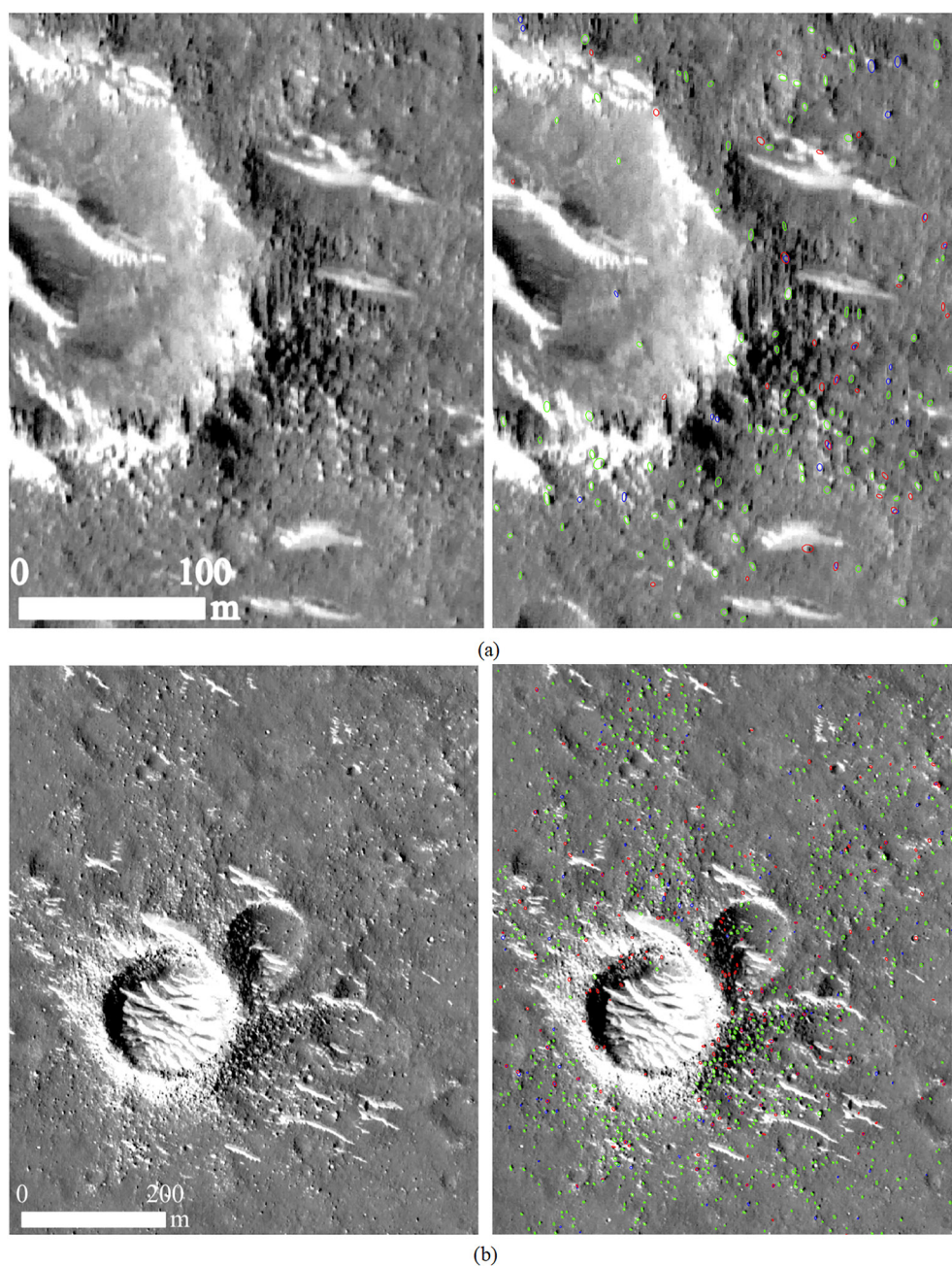


Figure 2. Rock detection results in the two selected regions based on high-resolution imaging experiment images. (a) Image ID: HX1-Or_GRAS_HiRIC-CCD3-F_SCI_N_20210318121707; (b) Image ID: HX1-Or_GRAS_HiRIC-CCD2-F_SCI_N_20210328182247.

images acquired by the Tianwen-1 orbiter correspond to three charge-coupled detectors (CCDs) per tile (Meng et al., 2021). Therefore, the three sub-images have slightly different brightness values. The Environment for Visualizing Images (ENVY) software was used to generate a mosaic among the tiles to eliminate the differences in brightness. Subsequently, the mosaic was upsampled by four times by applying the ESRGAN super-resolution algorithm (Wang et al., 2019) and cropped into patches with 416×416 pixels. The CNN-based method was implemented to automatically label rocks on images and had precision and recall rates of approximately 80% as

Table 2
Evaluation of Two Selected Regions

	Number of detections	Number of ground truth	True positives	False positives	False negatives	Classification precision	Classification recall
Region a	149	144	119	30	25	80%	83%
Region b	1029	968	811	218	157	79%	84%

shown in Table 2. Therefore, an extensive manual verification process was performed by a group of operators to enhance rock detection. The complete area was divided into several tiles, and the automatically detected results for each tile were individually checked by two operators to add missing rocks and eliminate false detections. Rocks that were labeled or confirmed by both operators were retained in the record as correct labels. The manual verification was accomplished by eight operators in approximately 1 week.

Figure 4 shows the rock abundance derived from the HiRIC images and IRTM (Christensen, 1986). The rock abundance of each pixel was calculated by counting the cumulative area of rocks versus the study area within the circle with a 450 m diameter. The resolution of the rock abundance map is 2.8 m/pixel. The mean and maximum rock abundance of the region shown in Figure 4a is 5% and 12%, respectively, which corresponds to a favorable condition for landing. Several differences are observed among the CCD images. The difference in the rock abundance caused by brightness discontinuity among different CCD images is 1%–2%. As shown in Figure 4b, the obtained results are consistent with the IRTM rock abundance (4%).

3.2. Rock Abundance Measured From Ground Images Acquired by the Rover

After the Zhurong rover landed on 15 May 2021, the navigation and terrain camera (NaTeCam) onboard the rover acquired images on the ground during its traversal. The NaTeCam comprises two identical cameras with a 27 cm baseline. At each station, 12 pairs of images can be obtained to observe the 360° environment and stitched into one panoramic image (Ding et al., 2022). On Sols 3–6 and Sol 40, the NaTeCam acquired panoramic images at the two locations, respectively. The two locations are located approximately 233 m apart (Figure 5a). The NaTeCam images were used for rock extraction and analysis of rock size–frequency distributions. The NaTeCam images were photogrammetrically processed to generate orthoimage mosaics (Wu et al., 2022). The spatial resolution of the NaTeCam imagery is about 1 mm/pixel close to the rover and 10 mm/pixel at a distance of 10 m. A unified spatial resolution of 5 mm/pixel was applied for the generated NaTeCam orthoimage mosaics as shown in Figures 5b and 5d. The dark areas in Figures 5b and 5d are occluded regions by the rover itself and dead zones from the NaTeCam's field of view. At these two locations, rocks distributed within a 20-m-diameter circular window centered at each location were manually labeled using the CraterHelper tool in the ArcMap software. These labels were used to derive the rock abundance values based on Equations 3 and 4.

The two locations have similar rock abundance values but different size–frequency distributions. The orthophotos and rock distributions at the two locations are shown in Figure 5. For the location imaged on Sols 3–6, 1,570 rocks with diameters ranging from 0.02 to 2.9 m were labeled. For the location imaged on Sol 40, 5,687 rocks with diameters ranging from 0.01 to 0.77 m were labeled. Although fewer rocks were recognized on Sols 3–6 than on Sol 40, the former location corresponds to a larger number of exposed bedrocks with a larger size, such as the bedrocks marked by ellipses with diameters of 2.9 and 1.2 m shown in Figures 5b and 5c. This finding indicates that during touchdown, the engine plumes of the lander probably moved small pebbles and cobbles away from the site, exposing several underground bedrocks. Most of the rocks, which have similar bedrock albedo and texture,

Table 3
High-Resolution Imaging Experiment Images Used at the Viking Lander 2 (VL2), MPF and InSight Landing Sites

ID	Center latitude	Center longitude	Emission angle	Incidence angle	Phase angle	Landing site
PSP_001501_2280	47.6735°	134.2995°	11.7418°	50.6099°	62.1424°	VL2
PSP_002391_1995	19.0879°	326.745°	18.5681°	54.4509°	72.9914°	MPF
ESP_061684_1845	4.4886°	135.616°	24.1293°	48.0951°	68.4424°	InSight

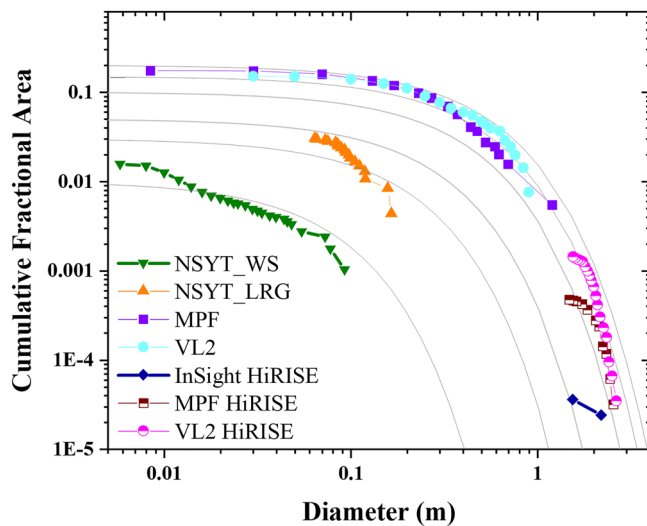


Figure 3. Cumulative fractional area covered by rocks versus rock diameter measured based on ground data and high-resolution imaging experiment (HiRISE) images of the testing landing sites. Curves show the exponential model size-frequency distribution of rock abundance of 1%, 3%, 5%, 10%, 15%, and 20%, as derived from (Equations 3 and 4; Golombek & Rapp, 1997). The VL2 data is from the NASA website. The MPF data is from Yingst et al. (2007). The InSight rock abundance (NSYT_WS and NSYT_LRG) is from Golombek, Kass, et al. (2020).

are widely spread around the rover, implying that these rocks originated from fractured bedrocks. The size-frequency distributions of rocks at the Zhurong landing site confirm a low rock abundance. Figure 6 shows the cumulative fractional area of rocks versus their diameters for the two regions. The rock abundance values at the locations imaged on Sols 3–6 and Sol 40 are approximately 7% and 5%, respectively. Because the two locations are only approximately 233 m apart, they are expected to correspond to the same landform and similar rock abundance. The different rock abundance values at these two locations indicate that the rocket engine plume displaced small pebbles and cobbles, and exposed large bedrocks increased the rock abundance by approximately 2% at the landing site. After excluding the 2.9 m bedrock from the CFA of Sols 3–6, the adjusted curve of Sols 3–6 matches the curve of Sol 40 well, as shown in Figure 6. A similar phenomenon has also been observed at the InSight landing site (Golombek, Warner, et al., 2020).

4. Surface Erosion Rate at the Zhurong Landing Site

The erosion rates of planetary surfaces are indicative of geological and climate history (Day & Anderson, 2021). This section analyzed the erosion rate in southern Utopia Planitia at the Zhurong landing site and its neighboring region (approximately 274 km²) as shown in Figure 4. First, two degradation states of craters were defined. Retention ages from degradation states and of craters with different diameters were estimated. Next, a fitting equation was derived from establishing the relationship among the rock abundance, crater retention ages, and crater diameters. The fitting result was used to determine the rock breakdown rate from the differences in rock abundance. Finally, the surface denudation rate was estimated from the filled volume of the degraded craters.

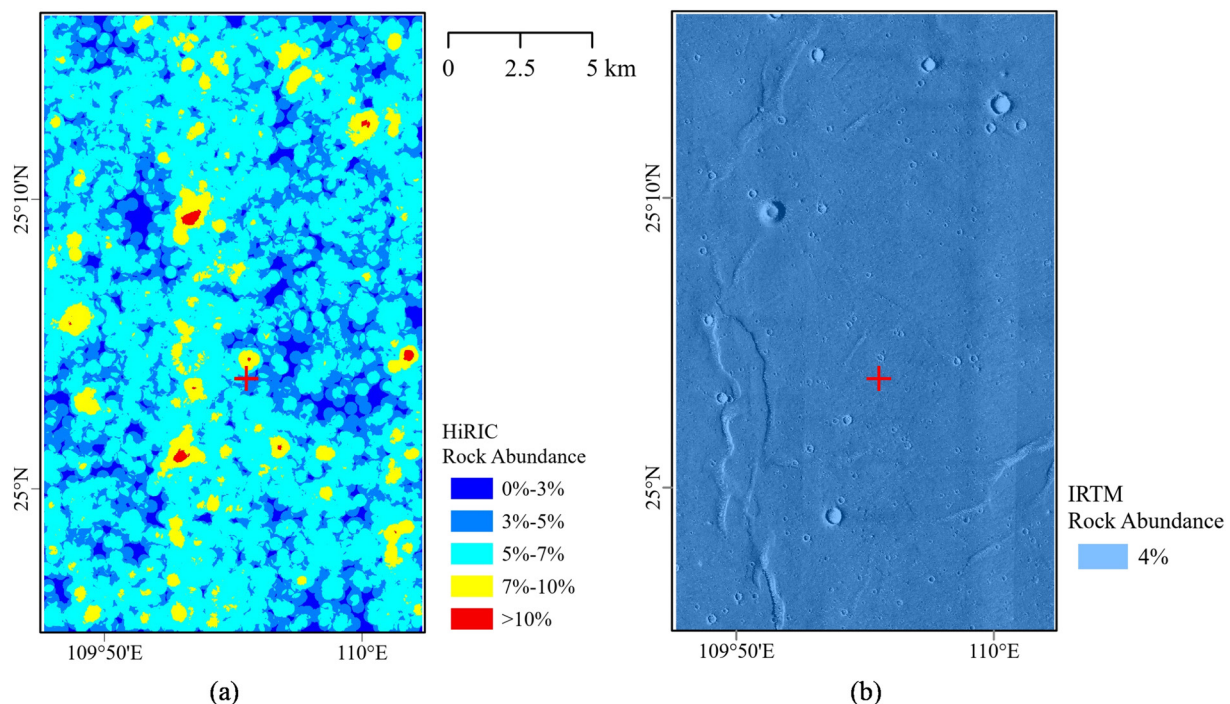


Figure 4. Rock abundance at the Zhurong landing site (red cross) and its neighboring region. (a) Rock abundance map from the high-resolution imaging camera (HiRIC) images (2.8 m/pixel); (b) Rock abundance map from the infrared thermal mapper (IRTM) data (60 km/pixel).

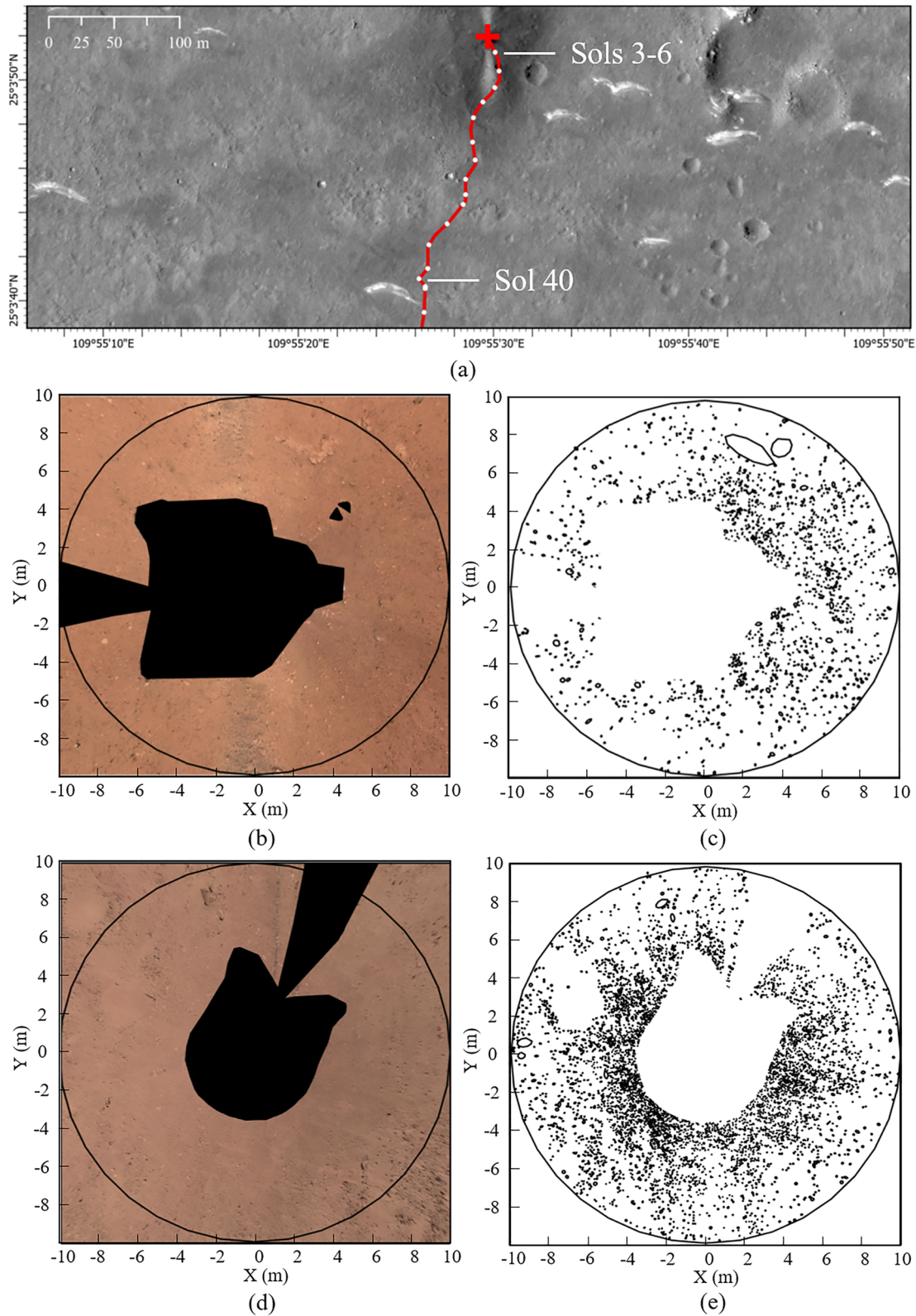


Figure 5. (a) Traversal of the Zhurong rover and two locations for rock analysis; (b) Orthophoto for Sols 3–6 generated using navigation and terrain camera images with a statistic area of 232 m²; (c) Rocks labeled on Sols 3–6; (d) Orthophoto for Sol 40 with a statistic area of 252.51 m²; (e) Rocks labeled on Sol 40.

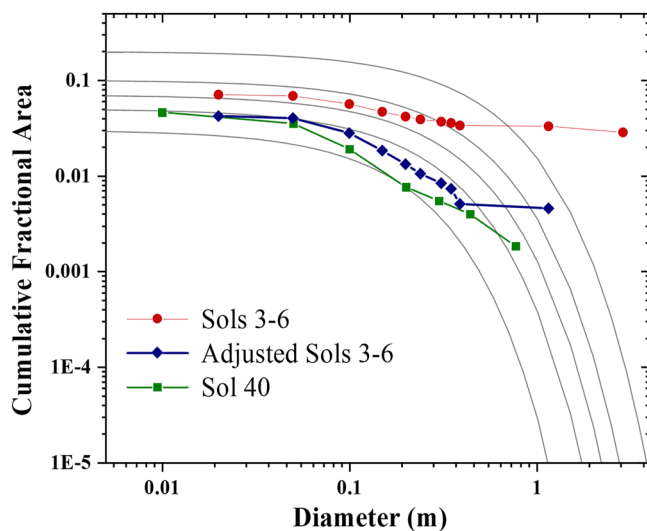


Figure 6. Cumulative fractional areas covered by rocks versus rock diameter at the Zhurong landing site on Sols 3–6 and Sol 40. The blue curve is adjusted from the Sols 3–6 curve by excluding the largest bedrock (the last data point on the red curve). The gray curves are theoretical distributions of the 3%, 5%, 7%, 10%, and 20% rock abundance values for reference.

4.1. Rock Abundance Versus Crater Retention Age and Diameter

The craters in the study area exhibit distinct morphologies and imply the extent, time, and rate of surface erosion. We used a machine-learning algorithm (Wang & Wu, 2019) to automatically detect craters from the HiRIC images covering the study area, followed by extensive manual checking to ensure data reliability. In total 14,357 craters with diameters ranging from 10 to 663 m were extracted for analysis. We defined two types of craters based on their morphological features: Class 1 craters have complete rims and visible blocky ejecta; Class 2 craters have partially or completely eroded rims. Figure 7a shows the distribution of craters in Class 1 (yellow) and Class 2 (blue) in the study area. Most craters have diameters less than 100 m; only 420 craters have diameters larger than 100 m. Figure 7b shows an example of the Class 1 crater, which represents the typical morphology of a fresh crater with clear rims and blocky ejecta surrounding the crater. Most Class 2 craters only have a circular shape, and their rims are partially or completely eroded, as the example shows in Figure 7c.

To quantitatively validate the classification criteria that distinguishes crater degradation states with morphological differences, the concept of relative degradation R (Forsberg-Taylor et al., 2004) is introduced here as follows:

$$R = \frac{H - h}{H}, \quad (5)$$

where H is the original depth of the crater when it was formed, and h is the current crater depth after surface erosion. The depth/diameter ratio of most craters when they were formed, including primary and secondary, is within 0.1–0.2 (Pike & Wilhelms, 1978). The value of H can then be estimated from the crater depth/diameter ratio. The current depth h can be measured from the digital elevation models (DEMs) generated from HiRISE or HiRIC images (Wu et al., 2021). We evaluated the relationship between R and the crater types (Class 1 or 2) using 5,906 craters with DEM data available in the study area. Figure 8 shows a clear statistical difference between the Class 1 and 2 craters. For Class 1 craters, the maximum relative depths are 0.66 and 0.83 for depth/diameter ratios of 0.1 and 0.2, respectively, indicating an effective classification.

To estimate the crater retention age, craters are grouped according to their diameters and degradation classes. Previous studies (Forsberg-Taylor et al., 2004; Hartmann, 1971) have stated that crater degradation is approximately a linear process, especially for small craters with diameters less than 1 km. A linear degradation indicates that small craters are more easily to be eroded and obliterated on the surface, and large craters could survive longer, even as old as the surface age.

A crater size–frequency distribution (CSFD) analysis was conducted to estimate the retention age of craters by using the CraterStats software (Michael & Neukum, 2010) and the Neukum–Ivanov chronology function (Neukum et al., 2001). Distinct secondary craters (e.g., chains and clustering) were excluded from the analysis. Figure 9a shows that the retention age is about 1.1 Ga using craters larger than 300 m, which is very close to the estimated age of 1.12 Ga of the Zhurong landing region in our previous work (Wu et al., 2022). The age estimated using craters with diameters ranging from 65 to 300 m is about 800 Ma, as shown in Figure 9b, indicating a possible subtle resurfacing event. These craters (65–300 m diameters) fit the production curve very well, indicating no obvious obliteration of craters within this diameter range. However, it is difficult to estimate the crater retention age within this diameter range because most craters have not been filled or destroyed, and impacts could happen at any time within the period of 800 Ma. Craters smaller than 65 m begin to show obvious deviations from the production curve, indicating that Class 2 craters with diameters of 65 m could be as old as 800 Ma. The average retention age of Class 2 craters with diameters ranging from 65 to 55 m is about 600 Ma as shown in Figure 9c. Class 1 craters with diameters of 65 to 55 m should have a similar filled depth to Class 2 craters with diameters of 42.9–36.3 m (calculated using the relative depth threshold of 0.66 and assuming the depth/diameter ratio of 0.1), of which the latter can be used to estimate the retention age of the former. According to Figure 9d, the average retention age of Class 1 craters with diameters of 65–55 m is about 270 Ma. Similarly, the average retention ages

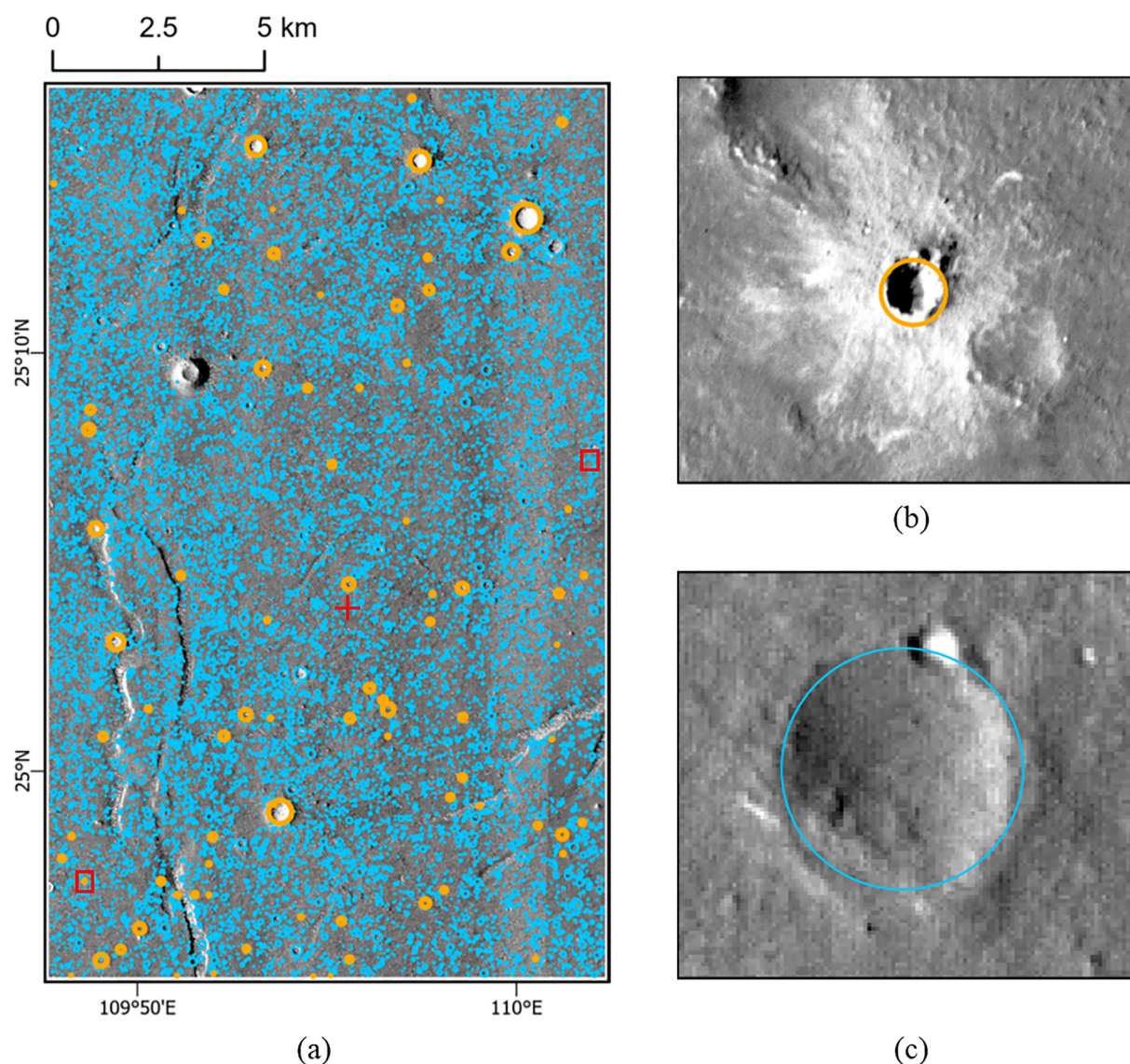


Figure 7. (a) Distribution of Class 1 (yellow) and Class 2 (blue) craters in the study area. The red cross in the middle indicates the Zhurong landing site, and the red boxes are the locations of examples; (b) An example of the Class 1 crater; (c) An example of the Class 2 crater.

for Class 1 and 2 craters with diameters ranging from 55 to 45 m can be estimated as shown in Figures 9e and 9f, respectively.

Several studies (Basilevsky et al., 2013; Ghent et al., 2014; Li & Wu, 2018; Wu et al., 2018) have indicated that rock distributions are inversely correlated with craters of different ages and diameters. We calculated the rock abundance associated with each crater for each diameter range within Classes 1 and 2. To obtain a reliable relationship between the rock abundance and crater age, the following steps were implemented in the statistical analysis. First, a circular buffer region (with a radius of two times of the crater radius) was established for each crater. The maximum rock abundance (refer to Figure 4) in the buffer region was extracted as the rock abundance associated with the crater for conservative consideration. In total, 83 Class 1 craters and 7,793 Class 2 craters at specific diameter ranges were involved in the analysis. Their retention ages estimated from each diameter range and the average rock abundances determined from all the craters within each diameter range are listed in Table 4.

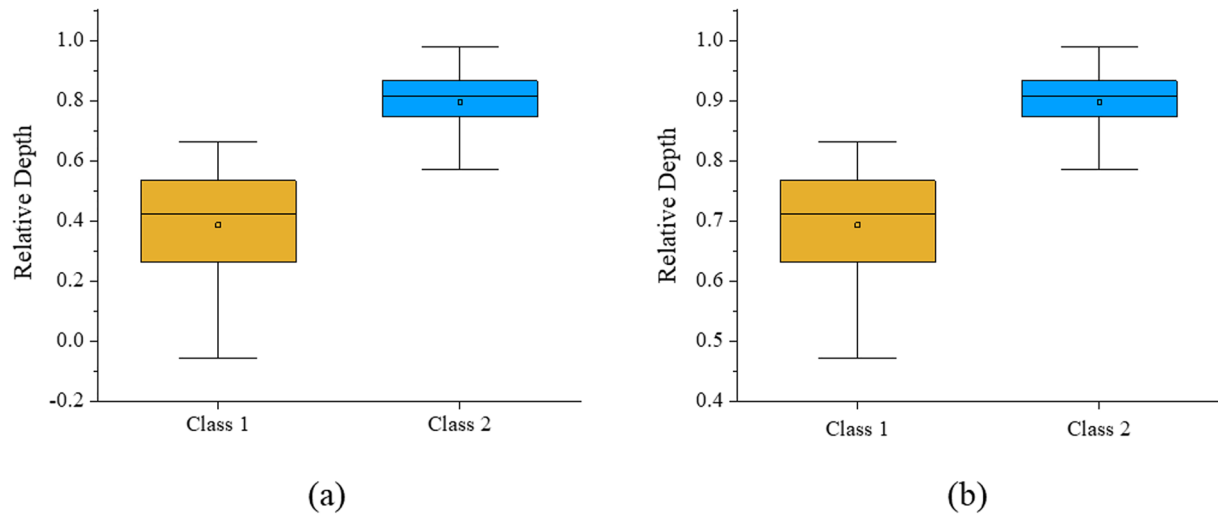


Figure 8. Relationship between crater relative depth and crater types. (a) Assuming a crater depth/diameter ratio of 0.1; (b) Assuming a crater depth/diameter ratio of 0.2.

The data listed in Table 4 were used to explore the relationship between rock abundance, crater retention age, and crater diameter. By assuming a linear model, the relationship is expressed as follows:

$$k = aD + bA + c, \quad (6)$$

where k is the rock abundance, D is the crater diameter in meters, and A is the crater retention age in Ma. The average crater diameter and rock abundance of each group are applied for the fitting. Using the five datasets listed in Table 4, the parameters were fitted with $a = 1.297 \times 10^{-4}$, $b = -2.135 \times 10^{-5}$ and $c = 0.064$. The R^2 value is 0.86. Figure 10 illustrates the fitting results. The fitted equation and parameters imply the following findings. First, the rock production rate by impacts is significantly larger than the erosion. Wu et al. (2018) reported a similar relationship between crater density and rock abundance on the lunar surface. Second, the intersect of 0.064 is the minimum rock abundance generated by impacts, which might be related to the surface and subsurface properties and compositions of the study area in southern Utopia Planitia.

4.2. Rock Breakdown Rate

The rock diameter is a dynamic value that varies owing to erosion processes such as breakdown and abrasion. These processes also change the frequency distributions of rocks of different diameters. According to Equations 3 and 4, large rocks and boulders occupy a larger percentage in high rock abundance regions than in low rock abundance conditions. Under a steady state in which no new rocks are generated, this phenomenon is indicative of a breakdown process in which a large rock disintegrates into several smaller pieces owing to erosion, and small rocks with a diameter less than a threshold are converted to fine grains as regolith. If the rock abundance values at two instances are known, the rock breakdown rate can be estimated.

The eroded diameter d of rocks can be calculated as follows. If the diameters of large rocks decrease due to erosion, small rocks with a diameter less than d are converted to regolith. Assuming that the probability density frequency (PDF) of the probability versus rock diameter is $f_n(D)$, where $f_n(D) = qe^{-qD}$ if we treat e^{-qD} in Equation 3 as a complementary cumulative distribution function, then the following expression is obtained:

$$k_1 \int_d^\infty f_n(D)_{k=k_1} = k_2 \int_0^{\infty-d} f_n(D)_{k=k_2}, \quad (7)$$

where k_1 and k_2 denote the rock abundance values, with $k_1 > k_2$. Equation 7 is a different representation of Equation 3, but two rock abundance values of the same area at different times are connected. Referring to Equation 3, the right side of Equation 7 equals the rock abundance k_2 and the left side is the cumulative fractional area of

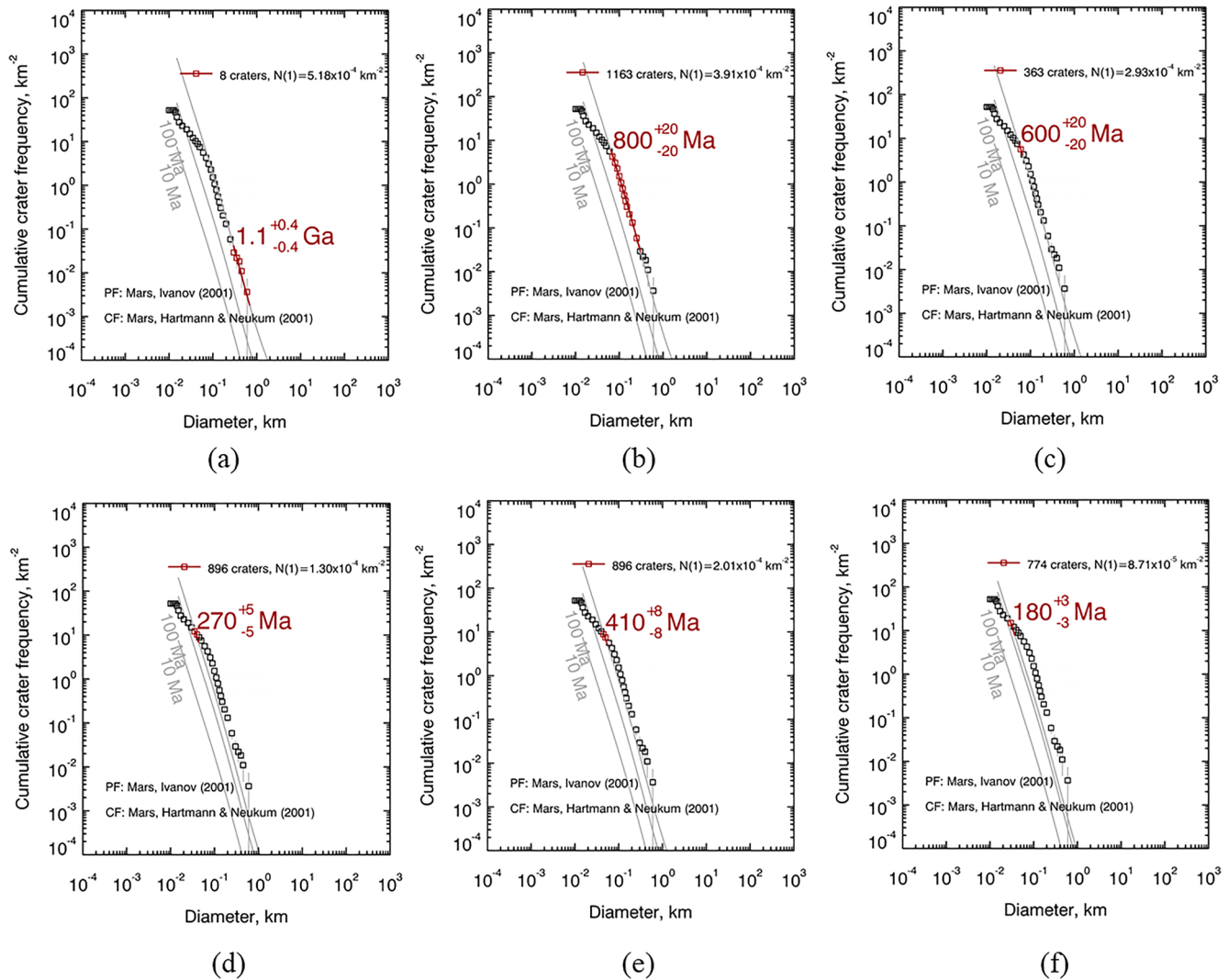


Figure 9. Crater size–frequency distribution (CSFD) plots and retention ages estimated using the chronology function defined by Neukum et al. (2001). The black squares represent the original data, and the red squares are craters used for age estimation. (a) CSFD plot for craters (>300 m) and estimated retention age; (b) CSFD plot for craters (300–65 m) and estimated retention age; (c) CSFD plot for Class 2 craters (65–55 m) and the estimated retention age; (d) CSFD plot for Class 1 craters (65–55 m) and estimated retention age; (e) CSFD plot for Class 2 craters (55–45 m) and estimated retention age; and (f) CSFD plot for Class 1 craters (55–45 m) and estimated retention age.

Table 4
Crater Retention Ages and Rock Abundances

Crater diameter (m)	Morphological classification	Diameter range for age estimate (m)	Crater retention age	Average rock abundance	Average crater diameter (m)
>300	Class 1	>300	1.1 Ga	0.091	393.5
65–55	Class 2	65–55	600 Ma	0.059	59.5
65–55	Class 1	42.9–36.3	270 Ma	0.074	58.2
55–45	Class 2	55–45	410 Ma	0.058	49.5
55–45	Class 1	36.3–29.7	180 Ma	0.061	51.2

rocks with diameters $\geq d$ is the eroded diameter during the time period and can be calculated as follows:

$$F_{k=k_1}(d) = k_2. \quad (8)$$

The erosion rate can be further derived from d . The erosion rate is estimated using craters with diameters of 65 m (with ages of 0 and 800 Ma) and 663 m (with ages of 0 and 1.1 Ga), of which the former indicates a representative crater size fitting well with the age estimation curve (refer to Figure 9b) in the study region and the latter is the largest crater in the study region. Their estimated rock abundances are derived using Equation 6. The calculated k_1 are 0.072 and 0.150, and k_2 are 0.055 and 0.127 for the two craters, respectively. Based on Equation 8, the calculated eroded diameter d is 0.059 and 0.069 m, respectively, implying that the rock breakdown rate in the Zhurong landing region ranges from 0.054 nm/y to 0.074 nm/y.

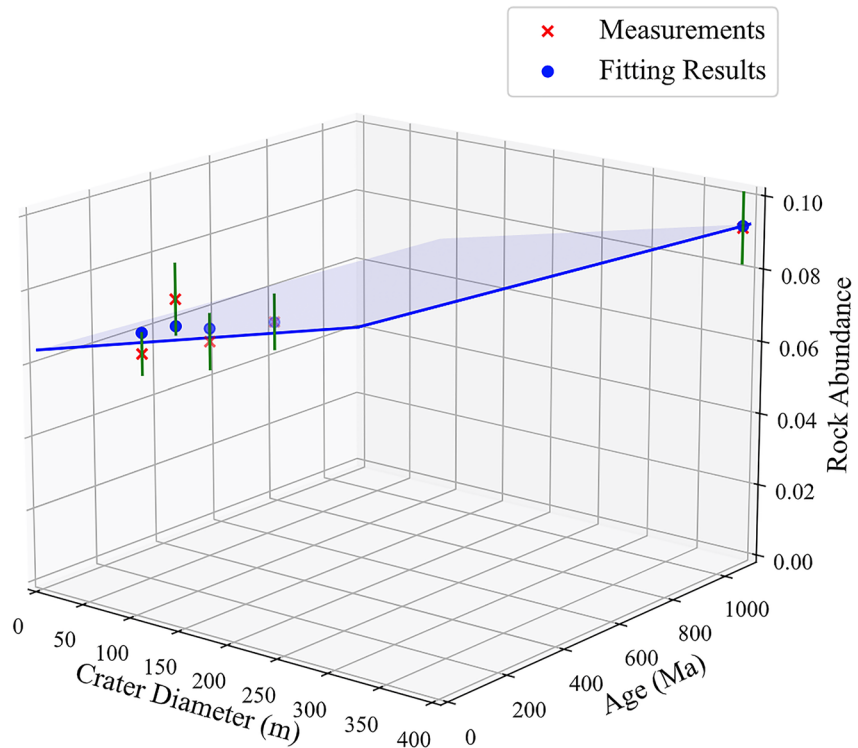


Figure 10. Results of the multivariable fitting. Blue points are the fitted rock abundance values using parameters in Equation 6, and red crosses are the actual measurements of rock abundance listed in Table 4. Green lines represent error bars of rock abundance.

4.3. Surface Denudation Rate

The redistribution of fine particles is expected to fill craters and flatten rims. The filled depth of craters is indicative of the resurfacing related to the eolian process. For a theoretical crater with a depth/diameter ratio of r , the filled volume of craters can be calculated by calculating the volume of the cone (Golombek et al., 2006):

$$V_c = \frac{r D_f \pi \left(\frac{D_f}{2}\right)^2}{3}, \quad (9)$$

where V_c and D_f denote the filled volume and floor diameter of the theoretical crater, respectively. The diameter of the floor, D_f , can be calculated as

$$D_f = D_c - p/r, \quad (10)$$

where D_c is the diameter of the crater, and p is the depth of the crater.

We evaluated 5,906 craters in the study area, with their depth and diameter information measured from the DEMs generated using HiRISE and HiRIC images (Wu et al., 2022). The region covered by these craters has an area of 144.96 km², and the volume of the filled craters is 0.017 and 0.033 km³, assuming r equals 0.1 and 0.2, respectively. In combination with the chronology result of 1.1 Ga, the surface denudation rate is approximately 0.104 nm/y to 0.209 nm/y, which suggests an extremely low erosion rate since the Amazonian period. It should be noted that the estimated rate is assumed from a local erosion and deposition process and does not consider the dust settling at the surface. The latter requires further investigation of the seasonal dust activities over the region.

5. Discussion

5.1. Rock Abundance in Southern and Northern Utopia Planitia

Before the Zhurong landing, the VL2 successfully landed in northern Utopia Planitia in 1976. Surface counts confirmed that the rock abundance is approximately 16%–19%, and several hypotheses of the rock source were proposed (Thomas et al., 1977). The first hypothesis is that the rocks and boulders are associated with the impacts of the Mie crater. The second hypothesis posits that they are remnant eolian deposits of the lava flow. The third hypothesis attributes them to the removal of deposits and the formation of lag deposits. The last hypothesis is that cemented ferricrete blocks beneath the surface were concentrated into lag deposits by deflation. The formation of lag deposits requires dozens of meters of deflation of concentrated rocks and boulders on the surface, and the VL2 landscape is deflated by more than 100 m to fulfill the requirements reported by Thomson and Schultz (2007). However, our erosion rate estimations do not support this resurfacing process, although the erosion rates are significantly higher in northern Utopia Planitia than those in the southern region. According to our estimations, the rocks and boulders were mainly generated from the Mie crater and subsequent smaller impacts and also originated from the lag deposits by deflation, consistent with previous work (Mutch et al., 1977). Similarly, impacts associated with small craters in southern Utopia Planitia are the primary sources of surface rocks and boulders, and the surface denudation concentrates the subsurface coarse deposits to a certain extent. The low rock abundance distribution on the surface is attributable to the lack of large craters.

5.2. Erosion Rates at the Zhurong Landing Site and Other Locations on Mars

Our findings indicate that the average breakdown rates of rocks and surface denudation rate are approximately 0.054 nm/y to 0.074 nm/y and 0.104 nm/y to 0.209 nm/y, indicative of an arid climate in the Amazonian period. The estimated rate is significantly lower than that in Earth environments (Levenson et al., 2017; Martin & Church, 1997) but higher than that for the lunar surface (Craddock & Howard, 2000). The obtained erosion rate estimations are comparable to those reported previously. The erosion rates from the late Hesperian to late Amazonian period are 0.03–100 nm/y, corresponding to extremely low values. Compared with the surface denudation rate of 100 nm/y reported for the VL2 landing site in northern Utopia Planitia by Arvidson et al. (1979), the value for the Zhurong landing site in southern Utopia Planitia is considerably smaller, and the surface denudation rate at the VL1 landing site in western Chryse Planitia is only 1 nm/y since the late Hesperian. For other landing sites, MPF and Spirit report similar estimations of 0.02 nm/y and 0.03 nm/y since 3.5 Ga and 3.1 Ga, respectively (Golombek & Bridges, 2000; Golombek et al., 2006), but the estimate for the Opportunity landing site is 1–2 orders of magnitude larger, from 1.3 nm/y to 15 nm/y. Haas et al. (2013) reported a considerably high rock breakdown rate of 3.5 m/Ma and surface denudation rate of 0.89 m/Ma on the fan in eastern Promethei Terra, suggestive of an abnormally high erosion rate in the Amazonian period. Since the late Hesperian, the other reported erosion rates have Mars been considerably lower than those of the Noachian to middle Hesperian (800–7700 nm/y) (Craddock et al., 1997; Craddock & Maxwell, 1993; Hartmann et al., 1999; Hynek & Phillips, 2001). Table 5 shows a summary of the erosion rates on Mars from the literature and this study.

6. Conclusions

This paper proposes a CNN-based method for rock extraction and analysis. The classification recall and precision rates of the proposed method applied to the HiRIC images are approximately 80%, corresponding to satisfactory performance. Moreover, the proposed method is tested against the ground measurement at several landing sites. The rock abundance estimated using the HiRISE images through the proposed algorithm agrees with the ground rock counts.

The proposed method is successfully applied for rock abundance analysis by using the HiRIC images covering the Zhurong landing site and its neighboring region. The results indicate that the mean rock abundance is approximately 5% over the region. Measurements from ground images collected by the Zhurong rover confirm a rock abundance of approximately 5% at the landing site, consistent with the orbital measurements from HiRIC images.

The rock abundance of craters is higher with increasing crater diameter but decreases with crater retention age. The estimated rock breakdown rate at the Zhurong landing region in southern Utopia Planitia ranges from 0.054 nm/y to 0.074 nm/y, and the surface denudation rate ranges from 0.104 nm/y to 0.209 nm/y. These values

Table 5
Summary of Erosion Rates on Mars

Location	Source	Age (Ga)	Erosion rate (nm/y)
Margaritifer Sinus	Craddock et al. (1997)	3.95–3.7	800
Arsia Mons caldera	Hartmann et al. (1999)	3.95–3.7	1000
Martian Highlands	Craddock and Maxwell (1993)	3.95–3.0	1295
Margaritifer Sinus, northern Arabia Terra	Hynek and Phillips (2001)	3.83–3.7	7700
Chryse Planitia	Arvidson et al. (1979)	3.2–0	1
Ares Vallis	Golombek and Bridges (2000)	3.1–0	0.02
Gusev plains	Golombek et al. (2006)	3.5–0	0.03
Meridiani Planum	Golombek et al. (2006)	3.0–0	1.3–15
Promethei Terra	Haas et al. (2013)	0.00125–0	890–3500
Southern Utopia Planitia	This study	1.1–0	0.054–0.209

imply that only eolian erosion is involved in the process. The conclusion is similar to that derived from other erosion rate estimations in the late Hesperian and Amazonian ages (Arvidson et al., 1979; Golombek et al., 2006; Golombek & Bridges, 2000; Grant et al., 2006). The low erosion rate indicates a dry climate in the Amazonian period.

This study represents the first attempt at estimating the rock abundance and erosion rates in southern Utopia Planitia. The proposed rock detection method can be applied for rock analysis at other locations on Mars based on high-resolution orbital images. The proposed method and findings can facilitate related scientific research on Mars, for instance, to identify abnormal erosions on the Martian surface and clarify the geological implications of rock abundance and erosions.

Data Availability Statement

The HiRIC and NaTeCam images can be obtained from the Lunar and Planetary Data Release System (GRAS, 2022) (<https://moon.bao.ac.cn/web/enmanager/mars1>) after the protection period which is typically 6 months after the data has been uploaded to the system. The MRO HiRISE data are available at NASA Planetary Data System (McEwen, 2007) (<https://hirise-pds.lpl.arizona.edu/PDS/>). The Viking rock data are available at NASA Planetary Data System (Simpson, 1998) (https://pds-geosciences.wustl.edu/missions/vlander/contents_rock.html). The MPF rock data can be found in the paper by Yingst et al. (2007). The InSight rock data can be found in Golombek, Kass, et al. (2020). The crater data and ground rock counts generated in this paper are available at Zenodo (Chen, 2022).

References

- Abadi, M., Barham, P., Chen, J., Chen, Z., Davis, A., Dean, J., et al. (2016). TensorFlow: A system for large-scale machine learning. In *Proceedings of the 12th USENIX Symposium on Operating systems design and Implementation (OSDI '16)* (pp. 265–283).
- Arthur, D., & Vassilvitskii, S. (2007). K-means++: The advantages of careful seeding. In *Proceedings of the Eighteenth Annual ACM-SIAM Symposium on Discrete Algorithms* (pp. 1027–1035). Society for Industrial and Applied Mathematics.
- Arvidson, R., Guinness, E., & Lee, S. (1979). Differential Aeolian redistribution rates on Mars. *Nature*, 278(5704), 533–535. <https://doi.org/10.1038/278533a0>
- Basilevsky, A. T., Head, J. W., & Horz, F. (2013). Survival times of meter-sized boulders on the surface of the Moon. *Planetary and Space Science*, 89, 118–126. <https://doi.org/10.1016/j.pss.2013.07.011>
- Bochkovski, A., Wang, C.-Y., & Liao, H.-Y. M. (2020). YOLOv4: Optimal speed and accuracy of object detection. ArXiv:2004.10934 [Cs.CV].
- Charalambous, C. (2014). *On the evolution of particle fragmentation with applications to planetary surfaces*. Imperial College London. PhD Thesis.
- Chen, Z. (2022). Datasets for rock abundance and erosion rate at Zhurong landing site on Mars [Dataset]. <https://doi.org/10.5281/zenodo.6504360>
- Christensen, P. R. (1986). The Spatial distribution of rocks on Mars. *Icarus*, 68(2), 217–238. [https://doi.org/10.1016/0019-1035\(86\)90020-5](https://doi.org/10.1016/0019-1035(86)90020-5)
- Craddock, R. A., & Howard, A. D. (2000). Simulated degradation of Lunar impact craters and a new method for age dating farside mare deposits. *Journal of Geophysical Research*, 105(E8), 20387–20401. <https://doi.org/10.1029/1999je001099>
- Craddock, R. A., & Maxwell, T. A. (1993). Geomorphic evolution of the Martian highlands through ancient fluvial processes. *Journal of Geophysical Research*, 98(E2), 3453–3468. <https://doi.org/10.1029/92je02508>
- Craddock, R. A., Maxwell, T. A., & Howard, A. D. (1997). Crater morphometry and modification in the Sinus Sabaeus and Margaritifer Sinus regions of Mars. *Journal of Geophysical Research*, 102(E6), 13321–13340. <https://doi.org/10.1029/97je01084>

Acknowledgments

This work was supported by grants from the China Academy of Space Technology (Project No: 17CPIT/HK0103) and the Research Grants Council of Hong Kong (RIF Project Nos: R5043-19 and PolyU 15210520). The authors thank the individuals who helped make the archive of the datasets publicly available and the reviewers who gave valuable comments on the study.

- Day, M., & Anderson, W. (2021). Wind erosion on Mars exposes ideal targets for sample return. *Geophysical Research Letters*, 48(2), e2020GL090580. <https://doi.org/10.1029/2020gl090580>
- Day, M., & Kocurek, G. (2016). Observations of an Aeolian landscape: From surface to orbit in Gale crater. *Icarus*, 280, 37–71. <https://doi.org/10.1016/j.icarus.2015.09.042>
- Ding, L., Zhou, R., Yu, T., Gao, H., Yang, H., Li, J., et al. (2022). Surface characteristics of the Zhurong Mars rover traverse at Utopia Planitia. *Nature Geoscience*, 15(3), 171–176. <https://doi.org/10.1038/s41561-022-00905-6>
- Forsberg-Taylor, N. K., Howard, A. D., & Craddock, R. A. (2004). Crater degradation in the Martian highlands: Morphometric analysis of the Sinus Sabaeus region and simulation modeling suggest fluvial processes. *Journal of Geophysical Research*, 109, E5. <https://doi.org/10.1029/2004je002242>
- Ghent, R. R., Hayne, P. O., Bandfield, J. L., Campbell, B. A., Allen, C. C., Carter, L. M., & Paige, D. A. (2014). Constraints on the recent rate of lunar ejecta breakdown and implications for crater ages. *Geology*, 42(12), 1059–1062. <https://doi.org/10.1130/g35926.1>
- Golombek, M., Huertas, A., Kipp, D., & Calef, F. (2012). Detection and characterization of rocks and rock size-frequency distributions at the final four Mars Science Laboratory landing sites. *Mars*, (7), 22.
- Golombek, M., Kass, D., Williams, N., Warner, N., Daubar, I., Piqueux, S., et al. (2020). Assessment of InSight landing site predictions. *Journal of Geophysical Research: Planets*, 125(8), e2020JE006502. <https://doi.org/10.1029/2020je006502>
- Golombek, M., Kipp, D., Warner, N., Daubar, I. J., Ferguson, R., Kirk, R. L., et al. (2017). Selection of the InSight landing site. *Space Science Reviews*, 211(1), 5–95. <https://doi.org/10.1007/s11214-016-0321-9>
- Golombek, M., & Rapp, D. (1997). Size-frequency distributions of rocks on Mars and Earth analog sites: Implications for future landed missions. *Journal of Geophysical Research*, 102(E2), 4117–4129. <https://doi.org/10.1029/96je03319>
- Golombek, M., Warner, N. H., Grant, J. A., Hauber, E., Ansan, V., Weitz, C. M., et al. (2020). Geology of the InSight landing site on Mars. *Nature Communications*, 11(1), 1014.
- Golombek, M. P., & Bridges, N. T. (2000). Erosion rates on Mars and implications for climate change: Constraints from the Pathfinder landing site. *Journal of Geophysical Research*, 105(E1), 1841–1853. <https://doi.org/10.1029/1999je001043>
- Golombek, M. P., Grant, J. A., Crumpler, L. S., Greeley, R., Arvidson, R. E., Bell, J. F., et al. (2006). Erosion rates at the Mars exploration rover landing sites and long-term climate change on Mars. *Journal of Geophysical Research*, 111(E12). <https://doi.org/10.1029/2006je002754>
- Golombek, M. P., Haldemann, A. F. C., Forsberg-Taylor, N. K., DiMaggio, E. N., Schroeder, R. D., Jakosky, B. M., et al. (2003). Rock size-frequency distributions on Mars and implications for Mars exploration rover landing safety and operations. *Journal of Geophysical Research*, 108(E12). <https://doi.org/10.1029/2002je002035>
- Golombek, M. P., Huertas, A., Marlow, J., McGrane, B., Klein, C., Martinez, M., et al. (2008). Size-frequency distributions of rocks on the northern plains of Mars with special reference to Phoenix landing surfaces. *Journal of Geophysical Research*, 113(E3), E00A09. <https://doi.org/10.1029/2007je003065>
- Golombek, M. P., Trussell, A., Williams, N., Charalambous, C., Abarca, H., Warner, N. H., et al. (2021). Rock size-frequency distributions at the InSight landing site, Mars. *Earth and Space Science*, 8(12), e2021EA001959. <https://doi.org/10.1029/2021ea001959>
- Goodfellow, I., Pouget-Abadie, J., Mirza, M., Xu, B., Warde-Farley, D., Ozair, S., et al. (2014). *Generative adversarial nets*. In *advances in neural information processing systems* (Vol. 27). Curran Associates, Inc.
- Grant, J. A., Arvidson, R., Bell, J. F., Cabrol, N. A., Carr, M. H., Christensen, P., et al. (2004). Surficial deposits at Gusev crater along Spirit rover traverses. *Science*, 305(5685), 807–810. <https://doi.org/10.1126/science.1099849>
- Grant, J. A., Wilson, S. A., Ruff, S. W., Golombek, M. P., & Koestler, D. L. (2006). Distribution of rocks on the Gusev plains and on Husband hill, Mars. *Geophysical Research Letters*, 33(16), L16202. <https://doi.org/10.1029/2006gl026964>
- GRAS. (2022). Lunar and planetary data Release system [Dataset]. GRAS. <https://moon.bao.ac.cn/web/enmanager/mars1>
- Greeley, R., Arvidson, R. E., Barlett, P. W., Blaney, D., Cabrol, N. A., Christensen, P. R., et al. (2006). Gusev crater: Wind-related features and processes observed by the Mars exploration rover Spirit. *Journal of Geophysical Research*, 111(E2). <https://doi.org/10.1029/2005je002491>
- Haas, T., de Hauber, E., & Kleinhans, M. G. (2013). Local late Amazonian boulder breakdown and denudation rate on Mars. *Geophysical Research Letters*, 40(14), 3527–3531. <https://doi.org/10.1002/grl.50726>
- Hartmann, W. K. (1971). Martian cratering III: Theory of crater obliteration. *Icarus*, 15(3), 410–428. [https://doi.org/10.1016/0019-1035\(71\)90119-9](https://doi.org/10.1016/0019-1035(71)90119-9)
- Hartmann, W. K., Malin, M., McEwen, A., Carr, M., Soderblom, L., Thomas, P., et al. (1999). Evidence for recent volcanism on Mars from crater counts. *Nature*, 397(6720), 586–589. <https://doi.org/10.1038/17545>
- Heet, T. L., Arvidson, R. E., Cull, S. C., Mellon, M. T., & Seelos, K. D. (2009). Geomorphic and geologic settings of the Phoenix Lander mission landing site. *Journal of Geophysical Research*, 114(E1), E00E04. <https://doi.org/10.1029/2009je003416>
- Howard, A. D., Breton, S., & Moore, J. M. (2016). Formation of gravel pavements during fluvial erosion as an explanation for persistence of ancient cratered terrain on Titan and Mars. *Icarus*, 270, 100–113. <https://doi.org/10.1016/j.icarus.2015.05.034>
- Hynek, B. M., & Phillips, R. J. (2001). Evidence for extensive denudation of the Martian Highlands. *Geology*, 29(5), 407–410. [https://doi.org/10.1130/0091-7613\(2001\)029<0407:efedot>2.0.co;2](https://doi.org/10.1130/0091-7613(2001)029<0407:efedot>2.0.co;2)
- Levenson, Y., Ryb, U., & Emmanuel, S. (2017). Comparison of field and laboratory weathering rates in carbonate rocks from an eastern Mediterranean drainage basin. *Earth and Planetary Science Letters*, 465, 176–183. <https://doi.org/10.1016/j.epsl.2017.02.031>
- Li, Y., & Wu, B. (2018). Analysis of rock abundance on Lunar surface from orbital and descent images using automatic rock detection. *Journal of Geophysical Research: Planets*, 123(5), 1061–1088. <https://doi.org/10.1029/2017je005496>
- Lin, T.-Y., Maire, M., Belongie, S., Hays, J., Perona, P., Ramanan, D., et al. (2014). Microsoft COCO: Common objects in context. In D. Fleet, T. Pajdla, B. Schiele, & T. Tuytelaars (Eds.), *Computer Vision – ECCV 2014* (pp. 740–755). Springer International Publishing. https://doi.org/10.1007/978-3-319-10602-1_48
- Martin, Y., & Church, M. (1997). Diffusion in landscape development models: On the nature of basic transport relations. *Earth Surface Processes and Landforms*, 22(3), 273–279. [https://doi.org/10.1002/\(sici\)1096-9837\(199703\)22:3<273::aid-esp755>3.0.co;2-d](https://doi.org/10.1002/(sici)1096-9837(199703)22:3<273::aid-esp755>3.0.co;2-d)
- McEwen, A. (2007). MRO High resolution Imaging science experiment (HiRISE) radiometrically-corrected, Geometrically-mapped Images [Dataset]. MROM-HIRISE-2-EDR-V1.0. <https://hirise-pds.lpl.arizona.edu/PDS/>
- Meng, Q., Wang, D., Wang, X., Li, W., Yang, X., Yan, D., et al. (2021). High resolution Imaging Camera (HiRIC) on China's first Mars exploration Tianwen-1 Mission. *Space Science Reviews*, 217(3), 42. <https://doi.org/10.1007/s11214-021-00823-w>
- Michael, G. G., & Neukum, G. (2010). Planetary surface dating from crater size–frequency distribution measurements: Partial resurfacing events and statistical age uncertainty. *Earth and Planetary Science Letters*, 294(3–4), 223–229. <https://doi.org/10.1016/j.epsl.2009.12.041>
- Mutch, T. A., Arvidson, R. E., Binder, A. B., Guinness, E. A., & Morris, E. C. (1977). The geology of the Viking Lander 2 site. *Journal of Geophysical Research*, 82(28), 4452–4467. <https://doi.org/10.1029/jso82i028p04452>
- Neukum, G., Ivanov, B. A., & Hartmann, W. K. (2001). Cratering records in the Inner Solar system in relation to the Lunar reference system. *Space Science Reviews*, 96(1), 55–86. https://doi.org/10.1007/978-94-017-1035-0_3

- Nowicki, S. A., & Christensen, P. R. (2007). Rock abundance on Mars from the thermal emission spectrometer. *Journal of Geophysical Research*, 112(E5), E05007. <https://doi.org/10.1029/2006je002798>
- Pajola, M., Rossato, S., Baratti, E., Pozzobon, R., Quantin, C., Carter, J., & Thollet, P. (2017). Boulder abundances and size-frequency distributions on Oxia Planum-Mars: Scientific implications for the 2020 ESA ExoMars rover. *Icarus*, 296, 73–90. <https://doi.org/10.1016/j.icarus.2017.05.011>
- Pike, R. J., & Wilhelms, D. E. (1978). Secondary-Impact Craters on the Moon: Topographic form and geologic process, 907–909. In *Presented at the Lunar and Planetary Science conference*.
- Simpson, R. A. (1998). Viking lander rock population archival data set [Dataset]. VLI/VL2M-LCS-5-ROCKS-V1.0.. https://pds-geosciences.wustl.edu/missions/vlander/contents_rock.html
- Thomas, M. A., Raymond, A. E., Alan, B. B., Guinness, E. A., & Elliot, M. C. (1977). The geology of the Viking lander 2 site. *Journal of Geophysical Research*, 92(28), 4452–4467. <https://doi.org/10.1029/jg082i028p04452>
- Thomson, B. J., & Schultz, P. H. (2007). The geology of the Viking Lander 2 site revisited. *Icarus*, 191(2), 505–523. <https://doi.org/10.1016/j.icarus.2007.05.011>
- Vago, J. L., Lorenzoni, L., Calantropio, F., & Zashchirinskiy, A. M. (2015). Selecting a landing site for the ExoMars 2018 mission. *Solar System Research*, 49(7), 538–542. <https://doi.org/10.1134/s0038094615070205>
- Wang, X., Yu, K., Wu, S., Gu, J., Liu, Y., Dong, C., et al. (2019). ESRGAN: Enhanced super-resolution generative adversarial networks. In L. Leal-Taixé & S. Roth (Eds.), *Computer Vision – ECCV 2018 workshops* (pp. 63–79). Springer International Publishing. https://doi.org/10.1007/978-3-030-11021-5_5
- Wang, Y., & Wu, B. (2019). Active machine learning approach for crater detection from planetary imagery and digital elevation models. *IEEE Transactions on Geoscience and Remote Sensing*, 57(8), 5777–5789. <https://doi.org/10.1109/tgrs.2019.2902198>
- Wu, B., Dong, J., Wang, Y., Li, Z., Chen, Z., Liu, W. C., et al. (2021). Characterization of the candidate landing region for Tianwen-1—China's first mission to Mars. *Earth and Space Science*, 8(6), e2021EA001670. <https://doi.org/10.1029/2021ea001670>
- Wu, B., Dong, J., Wang, Y., Rao, W., Sun, Z., Li, Z., et al. (2022). Landing site selection and Characterization of Tianwen-1 (Zhurong rover) on Mars. *Journal of Geophysical Research: Planets*, 127(4), e2021JE007137. <https://doi.org/10.1029/2021je007137>
- Wu, B., Huang, J., Li, Y., Wang, Y., & Peng, J. (2018). Rock abundance and Crater density in the Candidate Chang'E-5 landing region on the Moon. *Journal of Geophysical Research: Planets*, 123(12), 3256–3272. <https://doi.org/10.1029/2018je005820>
- Wu, B., Li, F., Hu, H., Zhao, Y., Wang, Y., Xiao, P., et al. (2020). Topographic and geomorphological mapping and analysis of the Chang'E-4 landing site on the far side of the Moon. *Photogrammetric Engineering & Remote Sensing*, 86(4), 247–258. <https://doi.org/10.14358/pers.86.4.247>
- Yang, C., Zhao, H., Bruzzone, L., Benediktsson, J. A., Liang, Y., Liu, B., et al. (2020). Lunar impact crater identification and age estimation with Chang'E data by deep and transfer learning. *Nature Communications*, 11(1), 6358. <https://doi.org/10.1038/s41467-020-20215-y>
- Yingst, R. A., Haldemann, A. F. C., Biedermann, K. L., & Monhead, A. M. (2007). Quantitative morphology of rocks at the Mars Pathfinder landing site. *Journal of Geophysical Research*, 112(E6), E06002. <https://doi.org/10.1029/2005je002582>